RSC Advances

PAPER

View Article Online
View Journal | View Issue

Check for updates

Cite this: *RSC Adv.*, 2019, **9**, 7635

Mechanism and stereoselectivity in NHC-catalyzed β-functionalization of saturated carboxylic ester†

Yan Li * and Zhiqiang Zhang

To understand the mechanism and origin of the stereoselectivity of the [3 + 2] annulation reaction between a carboxylic ester and an isatin generating spirooxindole lactone catalyzed by N-heterocyclic carbene (**NHC**), density functional theory (DFT) calculations have been carried out. DFT results indicate that the catalytic cycle begins with the coupling of the catalyst with benzotriazole ester, followed by α-deprotonation to produce the enolate intermediate. The subsequent 1,4-proton transfer affords the homoenolate intermediate. The next crucial step is the stereoselective C–C bond formation. Then proton transfer takes place leading to the formation of the lactone intermediate. Finally, the elimination of the catalyst furnishes the final product. The presence of 1-hydroxybenzotriazole (HOBt) dramatically accelerates the proton transfer step. More importantly, HOBt has a non-negligible impact on stereoselective C–C bond formation, and the *SR*-configured product is the major stereoisomer of the annulation product, which is in good agreement with the experimental observations. The differential π···π stacking, C–H···π, lone pair (LP)···π and repulsion interactions are found to be responsible for the stereoselectivity. The obtained mechanistic insights should provide valuable information for understanding the important roles of the **NHC** catalyst and HOBt additive and be helpful for designing better **NHC** catalysts for this kind of reaction.

Received 14th December 2018
Accepted 28th February 2019

DOI: 10.1039/c8ra10262g

rsc.li/rsc-advances

Open Access Article. Published on 06 March 2019. Downloaded on 2/20/2026 12:47:03 PM.
This article is licensed under a Creative Commons Attribution-NonCommercial 3.0 Unported Licence.

1. Introduction

As one of the most versatile and useful building blocks, saturated carbonyl compounds (*e.g.*, esters and aldehydes) have been widely used in fields as diverse as pharmacology, chemistry, and materials science. Because of their great synthetic value, the functionalization of saturated carboxylic compounds has attracted considerable attention.[1] However, the majority of the research work deals with either the carbonyl carbon atom or the α-carbon atom functionalization of saturated carbonyl compounds.[2] Developing direct and efficient methods for the β-functionalization of these compounds is highly desirable and is still a challenge for chemists.[3]

During the past few years, N-heterocyclic carbenes (**NHC**s) have become a hot topic of research due to their widely applications as ligands in organometallic catalysis[4] and in Lewis base catalysis.[5] More importantly, **NHC**s have received considerable attention because of their diverse applications in organocatalytic reactions with excellent efficiency, such as umpolung reaction, benzoin, Stetter, Mannich, Michael, cycloadditions, redox reactions, CO_2 fixation, cooperative catalysis and cascade reactions.[6] Indeed, many cycloaddition reactions using **NHC** catalysts affording various heterocycles have been reported, including the [2 + 2],[7] [2 + 4],[8] [3 + *n*] (*n* = 2, 3, 4),[9] and [4 + *n*] (*n* = 2, 3)[10] cycloadditions.

Recently, Xu *et al.* developed a catalytic protocol for the synthesis of spirooxindole lactones *via* β-functionalization of saturated carboxylic esters in tetrahydrofuran (THF) solvent at room temperature.[11] It was found that the reaction of carboxylic esters with isatins could be effectively catalyzed by using **NHC** as catalyst and 1-hydroxybenzotriazole (HOBt) as additive. Additional experiments showed that HOBt is important in the current reaction because the yields and enantio- and diastereo-selectivities were higher in the presence of HOBt as compared with that in the absence of HOBt.

However, the mechanism of the **NHC**-catalyzed [3 + 2] annulation reaction between carboxylic esters and isatins (Scheme 1) has not been studied theoretically until now. How does the catalytic reaction proceed? Which step is the stereo-controlling step? What role does the additive HOBt play? In this work, we will examine the **NHC**-catalyzed [3 + 2] annulation reaction between a carboxylic ester and an isatin using density functional theory calculations. We concentrate on the reaction mechanism as well as the origin of stereoselectivity. The objective of this work is to provide mechanistic insights for the catalyzed reaction shown in Scheme 1 and explain the enhanced

School of Chemical Engineering, University of Science and Technology Liaoning, Anshan 114051, P. R. China. E-mail: snow2007liyan@163.com; Fax: +86-412-5929627; Tel: +86-18741219506

† Electronic supplementary information (ESI) available. See DOI: 10.1039/c8ra10262g

Open Access Article. Published on 06 March 2019. Downloaded on 2/20/2026 12:47:03 PM.
This article is licensed under a Creative Commons Attribution-NonCommercial 3.0 Unported Licence.

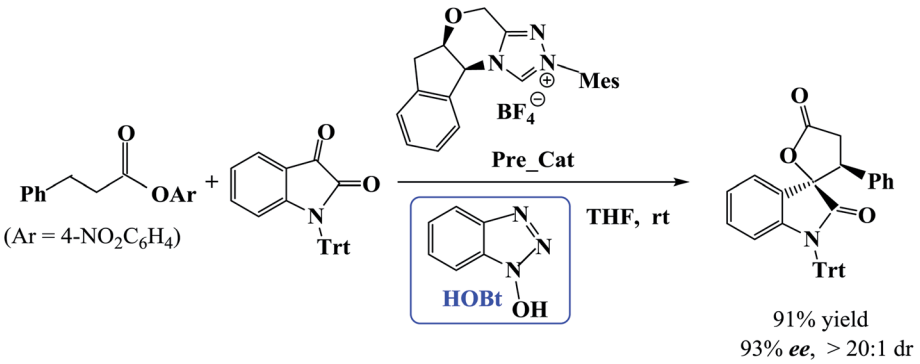

Scheme 1 NHC-catalyzed [3 + 2] annulation reaction.

stereoselectivity in the presence of HOBt in comparison to that in its absence.

2. Computational methods

Geometries of all the structures involved in the reaction were optimized using the M06-2X functional[12] with the 6-31G(d) basis set. Previous studies have confirmed the reliability of the chosen M06-2X functional.[13] Frequency calculations were performed in order to check the minimum has all real frequencies while the transition state has one and only one imaginary frequency and to obtain thermodynamic corrections at 298.15 K and 1 atm pressure. In order to confirm the connection of the transition states and the desired minima, intrinsic reaction coordinate (IRC) calculations were also performed.[14] To account for solvent effect, single-point energy calculations were carried out at the M06-2X/6-311++G(d,p) level in the solvent phase modeled by the Cramer–Truhlar continuum solvation model SMD[15] in tetrahydrofuran (THF, $\varepsilon = 7.43$). To assign the atomic charges, natural bond orbital (NBO) analyses were also carried out.[16] All calculations were carried out with the Gaussian 09 software package.[17]

3. Results and discussion

3.1 Reaction mechanism

In this section, we present and discuss the detailed results for the [3 + 2] cycloaddition reaction between 4-nitrophenyl 3-phenylpropanoate and isatin depicted in Scheme 1. On the basis of our calculation results, the detailed mechanism for the whole catalytic cycle is presented in Scheme 2. Before considering the possible reaction pathways of the current reaction, we explore first the actual catalyst in the current reaction. As shown in Scheme 2, in the presence of cesium carbonate Cs_2CO_3, the catalyst precursor **Pre_Cat** will undergo deprotonation to form the active **NHC** catalyst and release bicarbonate anion HCO_3^-.[18] Experimentally, 4-nitrophenyl 3-phenylpropanoate was used as one substrate (isatin as the other substrate) and 1-hydroxybenzotriazole (HOBt) as an additive. Computationally, we use the benzotriazole ester, depicted in Scheme 2 as one starting reactant because benzotriazole ester can be generated through the reaction of 4-nitrophenyl 3-phenylpropanoate with HOBt.

As presented in Scheme 2, the catalytic reaction proceeds *via* six steps: (1) the additon of the active catalyst **NHC** to benzotriazole ester **R1** to form the acyl azolium intermediate **IM1** and release OBt^-; (2) the deprotonation of the α-C–H in **IM1** to generate the enolate intermediate **IM2**; (3) the proton transfer of **IM2** leads to the homoenolate intermediate **IM3**; (4) the stereoselective carbon–carbon bond formation process which can be achieved from the addition of isatin **R2** to **IM3** leading to intermediate **IM4**; (5) the proton transfer followed by the intramolecular lactonization will eventually provide access to the five membered ring intermediate **IM6**, and (6) the elimination of the **NHC** catalyst yields the spirooxindole lactone product **P** with two chiral carbon atoms. The corresponding free energy profiles and optimized structures are shown in Fig. 1 (steps I–III) and 2 (steps IV–VI). In the following part, the reaction mechanism will be examined in greater detail.

Step I: addition of catalyst NHC to benzotriazole ester R1. As shown in Fig. 1, the reaction is initiated by the coupling of the **NHC** catalyst with benzotriazole ester **R1** leading to the formation of intermediates **IM01** and **IM01-1** *via* the respective transition states **TS1** and **TS1-1**. The calculated free energy barriers of **TS1** and **TS1-1** are 15.6 kcal mol^{-1} and 18.3 kcal mol^{-1}, respectively. The relative free energy of **IM01** and **IM01-1** are 6.3 and 9.7 kcal mol^{-1}, respectively. Clearly, formation of intermediate **IM01** is both kinetically and thermodynamically much more favorable than **IM01-1**. Therefore, the description herein focuses on the reaction pathways associated with intermediate **IM01**. As shown in Fig. 1, for the transformation of **TS1** → **IM01**, the distance of C1–C2 bond shortens from 2.239 Å to 1.560 Å, while that of C2–O bond increases from 1.447 Å to 1.658 Å. These results demonstrate that the formation of C1–C2 bond is occurred together with the cleavage of C2–O bond. Subsequent dissociation of OBt^- from **IM01** leads to the acyl azolium intermediate **IM1**.

Scheme 3 shows the NBO charge analysis results. As can be seen from Scheme 3, for **Cat** + **R1** → **IM01** process, the positive charge value on the C1 atom increases from 0.148*e* to 0.414*e*, while that on the C2 atom decreases from 0.840*e* to −0.041*e*. Furthermore, the negative charge value on the N atom decreases from −0.489*e* to −0.415*e*, while that of the carbonyl oxygen O3 atom increases from −0.543*e* to −0.909*e*. These results indicate

 This journal is © The Royal Society of Chemistry 2019

Open Access Article. Published on 06 March 2019. Downloaded on 2/20/2026 12:47:03 PM.
This article is licensed under a Creative Commons Attribution-NonCommercial 3.0 Unported Licence.

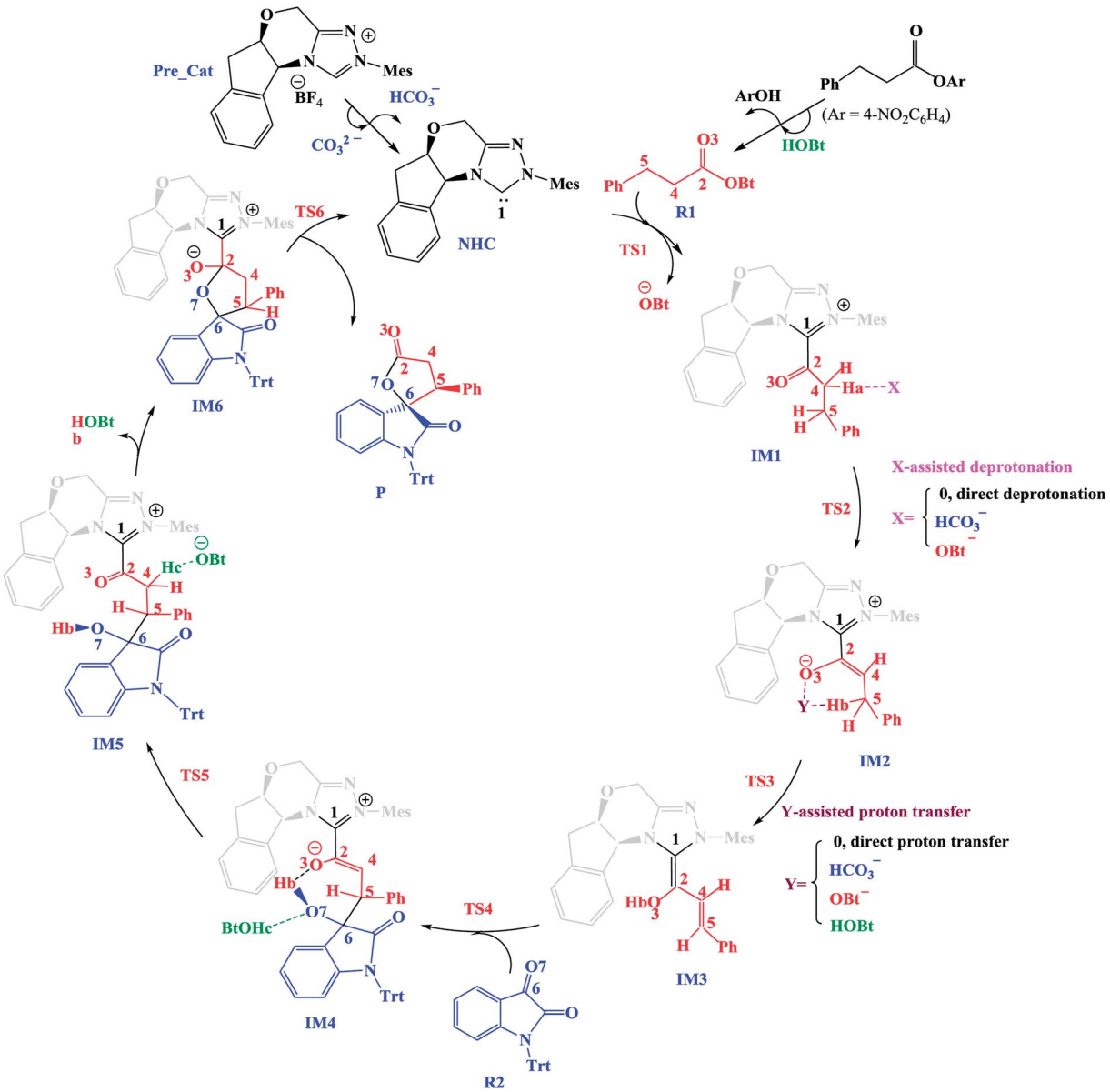

Scheme 2 The key steps involved in the NHC-catalyzed [3 + 2] annulation reaction.

that the electron density is transferred from **Cat** to **R1** during the process of **Cat** + **R1** → **IM01**.

Step II: α-C–H deprotonation. From intermediate **IM1**, α-C–H deprotonation occurs to generate the enolate intermediate **IM2**. Many computational studies have shown that the mediators assisted deprotonation favors the direct deprotonation.[19] In this work, three possibilities including direct, OBt^- and HCO_3^- assisted deprotonation have been investigated.

(1) Direct deprotonation. For direct deprotonation, we can not locate the corresponding transition state despite lots of attempts. We performed relax potential energy scan for the C4–Ha bond. The corresponding pointwise potential curve was provided in Fig. S1 in the ESI.† Fig. S1† clearly shows that the energy keeps increasing when the Ha atom getting farther from the C4 atom of **IM1**. The high energy barrier estimated for direct deprotonation process (~70 kcal mol^{-1}), indicates that the direct deprotonation pathway is kinetically unfeasible. In view of this, a mediator assisted deprotonation, facilitated by the previously formed OBt^- (or HCO_3^-) has been examined.

(2) OBt^- assisted deprotonation. The anion OBt^- generated in the first step can remove the hydrogen atom (Ha) in **IM1** *via* the transition state **TS2** to generate intermediate **IM2**. The calculated free energy barrier is 2.4 kcal mol^{-1} for **TS2** with respect to **IM1**, demonstrating that the OBt^- mediated deprotonation of α-C–H is a fast process under the experimental conditions. During this process (**IM1** → **TS2** → **IM2**), the distance of C4–Ha bond is elongated from 1.099 Å to 1.372 Å (**IM1** → **TS2**), whereas the distance of Ha–O bond is shortened from 1.245 Å, to 0.973 Å (**TS2** → **IM2** + **OBt**). These results indicate that the deprotonation process is completed. The transformation from **IM1** to **IM2**

Open Access Article. Published on 06 March 2019. Downloaded on 2/20/2026 12:47:03 PM.
This article is licensed under a Creative Commons Attribution-NonCommercial 3.0 Unported Licence.

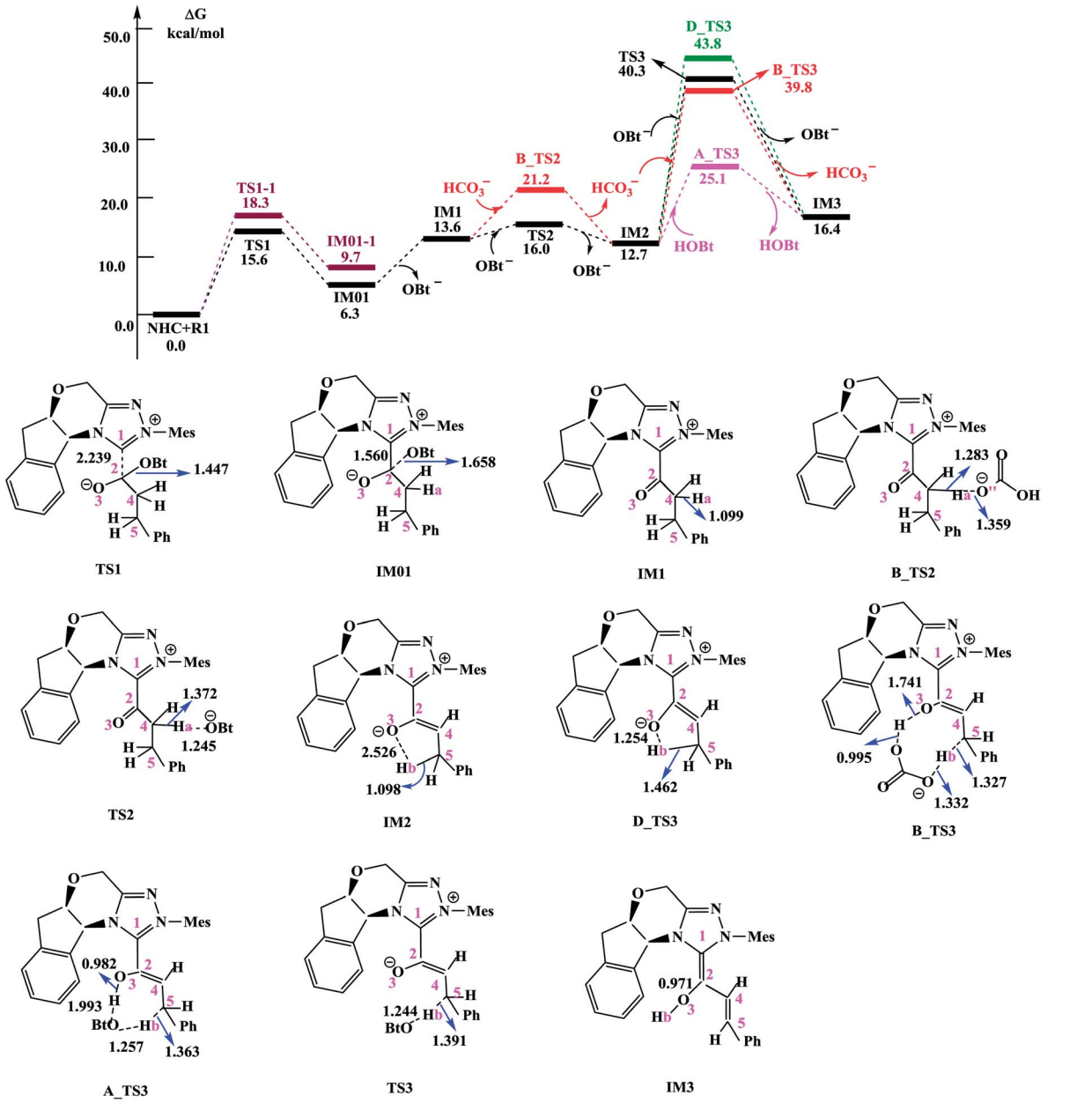

Fig. 1 Free energy profile obtained at SMD(THF)/M06-2X/6-311++G(d,p) level (kcal mol^{-1}) and optimized structures for steps I–III. Bond lengths are given in Å.

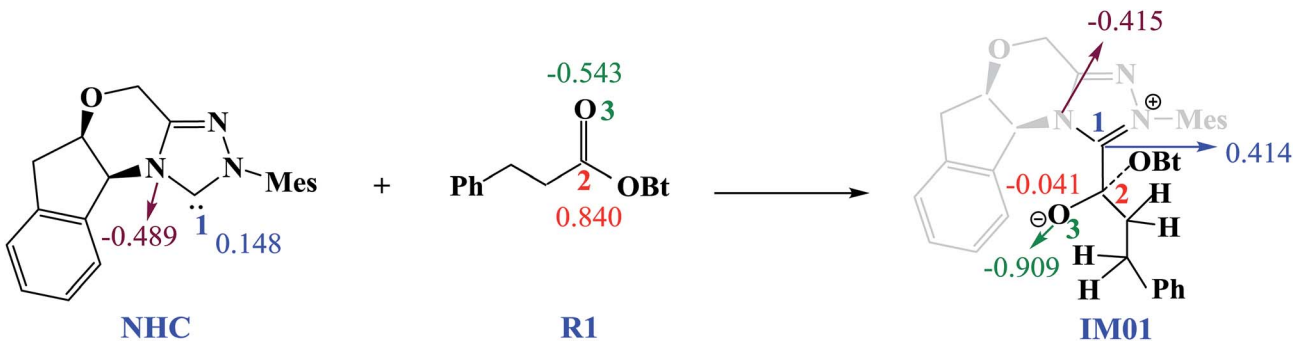

Scheme 3 The NBO charges of selected atoms in **NHC**, **R1** and **IM01** (units of *e*).

This journal is © The Royal Society of Chemistry 2019

Open Access Article. Published on 06 March 2019. Downloaded on 2/20/2026 12:47:03 PM.
This article is licensed under a Creative Commons Attribution-NonCommercial 3.0 Unported Licence.

is found to be slightly exergonic with a reaction energy of −0.9 kcal mol^{-1}.

(3) HCO_3^- assisted deprotonation. In another possibility, the previously formed HCO_3^- was used as promoter. The energy barrier calculated for the HCO_3^- assisted deprotonation is 7.6 kcal mol^{-1} *via* **B_TS2**. As shown in Fig. 1, the distance of C4–Ha bond increases from 1.099 Å in **IM1** to 1.283 Å in **B_TS2**, while that of Ha–O″ bond decreases from 1.359 Å in **IM1** to 0.968 Å in H_2CO_3.

Taken together, the mediators (BtO^- and HCO_3^-) promote the deprotonation process. The most favored proton transfer pathway is found to be that from **IM1** to **IM2** *via* **TS2** with the assistance of OBt^-.

Step III: 1,4-proton transfer. The 1,4-proton transfer of **IM2** forms intermediate **IM3**. Similar to the discussion of step II, both direct and mediator (HCO_3^-, BtO^- and HOBt) promoted proton transfer processes have been investigated.

For direct 1,4-proton transfer, migration of the Hb atom connected to C5 atom to O3 atom *via* the corresponding five-membered ring transition state **D_TS3** with a free energy barrier of 31.1 kcal mol^{-1} (43.8 kcal mol^{-1} with respect to reactants) (Fig. 1). Therefore, direct 1,4-proton transfer in intermediate **IM2** is a kinetically inaccessible process under the experimental conditions.

We also calculated the HCO_3^- and OBt^- assisted proton transfer. The corresponding energy profiles are also presented in Fig. 1. However, the high activation energies of **B_TS3** (39.8 kcal mol^{-1} relative to reactants, associated with the HCO_3^- mediated proton transfer) and **TS3** (40.3 kcal mol^{-1} relative to reactants, associated with the OBt^- mediated proton transfer) indicate that the mediator (HCO_3^- and BtO^-) has minimal effects on the proton transfer event. Thus these pathways are also kinetically unfavorable, and can be ruled out.

Experimentally, HOBt was used as an additive, promoting us to investigate the HOBt assisted proton transfer process. According to our calculation results, the 1,4-proton transfer proceeds *via* the seven-membered ring transition state **A_TS3** leading to the formation of the homoenolate intermediate **IM3** in the presence of HOBt (Fig. 1). Computational results show that the transition state for this process (**A_TS3** (25.1 kcal mol^{-1})) is much lower in energy than those of the unassisted and the BtO^- and HCO_3^- assisted proton transfer processes (*i.e.*, **D_TS3** (43.8 kcal mol^{-1}), **B_TS3** (39.8 kcal mol^{-1}) and **TS3** (40.3 kcal mol^{-1})). As can be seen from Fig. 1, the Hb atom migrates from C5 to O, at the same time, the H atom transfers from O to O3 *via* the seven-membered ring transition state **A_TS3**. The bond distances of C5–Hb, Hb–O, O–H and O3–H in **A_TS3** are 1.363, 1.257, 1.993 and 0.982 Å, respectively, indicating the HOBt mediated 1,4-proton transfer occurs in a concerted manner but not synchronous.

Step IV: the stereoselective C–C bond formation. The fourth step is the stereoselective determining step, which involves the addition of the C5 atom of **IM3** to the C6 atom of **R2** leading to the formation of C–C bond. As depicted in Scheme 4, four stereochemically distinct attack modes *i.e.* (*Re*, *Re*), (*Re*, *Si*), (*Si*, *Re*) and (*Si*, *Si*) were located resulting into the formation of intermediates **IM4(RR&RS&SR&SS)**, which have two chiral carbon atoms (*i.e.,* C5 and C6). It should be noted that the formation of the C5–C6 bond is concerted with a proton transfer of the enolate proton to the isatin moiety leading to the formation of intermediate **IM4**. According to experiments, improved enantioselectivity could be achieved when HOBt was used as an additive,[11] both the non- and HOBt-assisted C–C bond formation pathways have thus been explored.

In the absence of HOBt, the activation energy barriers of this step *via* transition states **D_TS4(RR&RS&SR&SS)** are 13.2/20.2/14.0/17.9 kcal mol^{-1} (29.6/36.6/30.4/34.3 kcal mol^{-1} with respect to reactants), as shown in Fig. S2.† Considering that the activation energy barrier of **D_TS4(RR)** is lower than those of **D_TS4(RS&SR&SS)**, the reaction pathway associated with **D_TS4(RR)** should be more favorable than the other pathways. Therefore, the dominant product in the absence of HOBt should be the *RR* configuration product. This is inconsistent with the experimental results. The experimentally observed major product without the use of HOBt was the SR-stereoisomer of the cycloaddition product.[11] Considering this inconsistency, more experimental studies are expected to be necessary to better understand the stereoselectivity associated with the reaction, depicted in Scheme 1 in the absence of HOBt.

Since HOBt was used as an additive in experiment,[11] it might assist in this C–C bond formation. We thus have included an explicit molecule of HOBt in this step to form intermediate **IM4**. Fig. 2 shows that the free energy barriers of this step in the presence of HOBt *via* transition states **TS4(RR&RS&SR&SS)** are 9.8/10.2/7.9/12.1 kcal mol^{-1} (26.2/26.6/24.3/28.5 kcal mol^{-1} relative to reactants), which is found to be lower than the transition states in the absence of HOBt (for details see the ESI, Fig. S2†). To understand this result, we examined the non and HOBt assisted transition state (**D_TS4** and **TS4**) structures (shown in Fig. S3†). As depicted in Fig. S3,† additional interactions such as O–H···O and O–H···N are present in the HOBt-assisted transition state compared to the unassisted transition state. These interactions are depicted as follows: O–H···O (a, b, c and d) and O–H···N (e). Moreover, Fig. 2 clearly shows that the energy barrier of **TS4(SR)** is remarkably lower than those of other configuration transition states (*i.e.*, **TS4(RR)**, **TS4(RS)** and **TS4(SS)**), for simplicity of presentation, we discuss the reaction pathways starting from **IM4(SR)** here (as shown in Fig. 2). Results for the less favorable pathways which feature *RR*/*RS*/*SS*-configuration are provided in the ESI (Fig. S4†). Intrinsic reaction coordinate (IRC) results for transition state **TS4(SR)** reveal that the C5–C6 bond formation occurs along with the Hb atom migration from O3 to O7, leading to intermediate **IM4(SR)**. From **TS4(SR)** to **IM4(SR)**, the distance of C5–C6 bond changes from 2.502 Å to 1.570 Å, at the same time, the distance of O3–Hb bond increases from 0.975 Å to 1.426 Å, while the Hb–O7 bond shortens from 2.136 Å to 1.051 Å. The above structural analysis indicates that the C5–C6 bond formation is accompanied by the transformation of the Hb atom (from O3 to O7).

Step V: the proton transfer and intramolecular lactamization. As shown in Fig. 2, intermediate **IM4(SR)** undergoes consecutive proton transfer and intramolecular lactonization to reach intermediate **IM6(SR)**. First, the proton Hc transfers to the C4 atom generates intermediate **IM5(SR)**. This proton

Open Access Article. Published on 06 March 2019. Downloaded on 2/20/2026 12:47:03 PM.
This article is licensed under a Creative Commons Attribution-NonCommercial 3.0 Unported Licence.

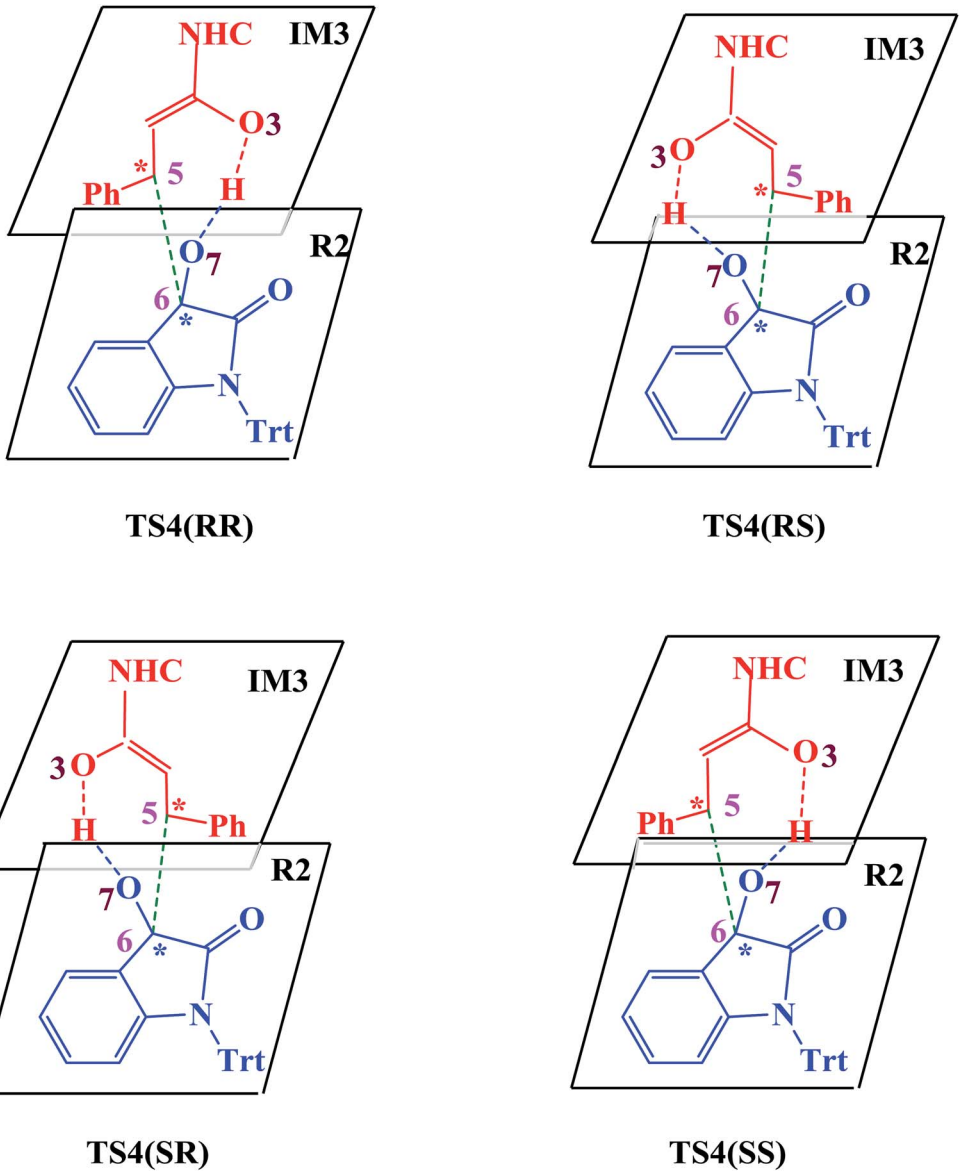

Scheme 4 Four attack modes involved in the stereoselectivity determining step (the hydrogen atoms are omitted).

transfer step *via* transition state **TS5(SR)** has an activation energy of 10.2 kcal mol^{-1}. For **IM4(SR)** → **TS5(SR)** → **IM5(SR)** reaction course, the bond distance of O'–Hc is elongated from 1.300 Å in **TS5(SR)** to 2.058 Å in **IM5(SR)**, while that of Hc–C4 is shortened from 1.330 Å in **TS5(SR)** to 1.111 Å in **IM5(SR)**. Subsequently, lactonization of **IM5(SR)** generates the slightly more stable intermediate **IM6(SR)**. Note that we can not locate the corresponding transition state despite lots of attempts. From **IM5(SR)** to **IM6(SR)**, the distance of C2–O7 bond shortens from 2.804 Å to 1.523 Å.

Step VI: formation of the cycloaddition product. In the final step, **NHC** catalyst releases from intermediate **IM6(SR)** affording the final cycloaddition product **P(SR)** through the transition state **TS6(SR)** with an activation energy of 6.0 kcal mol^{-1}. As shown in Fig. 2, the distance of C1–C2 bond is elongated from 1.546 Å in **IM6(SR)**, to 2.031 Å in **TS6(SR)**.

3.2 Origin of selectivity

As shown in Fig. 2 and discussed above in step IV, the addition of the homoenolate intermediate **IM3** to isatin **R2** leading to the formation of C–C bond is the stereoselectivity-determining step. Consequently, transition states **TS4(RR)**, **TS4(RS)**, **TS4(SR)** and **TS4(SS)** are found to be responsible for determining the stereoselectivity of the entire reaction. The activation energy barriers for generating the RR/RS/SR/SS configuration products *via* **TS4(RR/RS/SR/SS)** are calculated to be 26.2/26.6/24.3/28.5 kcal mol^{-1} (the energy difference between **TS4(RR/RS/SR/SS)** and reactants). Obviously, the *SR*-configurational product **P(SR)** is the major product, agrees well with the experimental observations. Based on the Curtin–Hammett Principle,[20] the product distribution is determined by the standard free energy difference of the stereoselectivity-determining transition states. The energy difference between

 This journal is © The Royal Society of Chemistry 2019

Open Access Article. Published on 06 March 2019. Downloaded on 2/20/2026 12:47:03 PM.
This article is licensed under a Creative Commons Attribution-NonCommercial 3.0 Unported Licence.

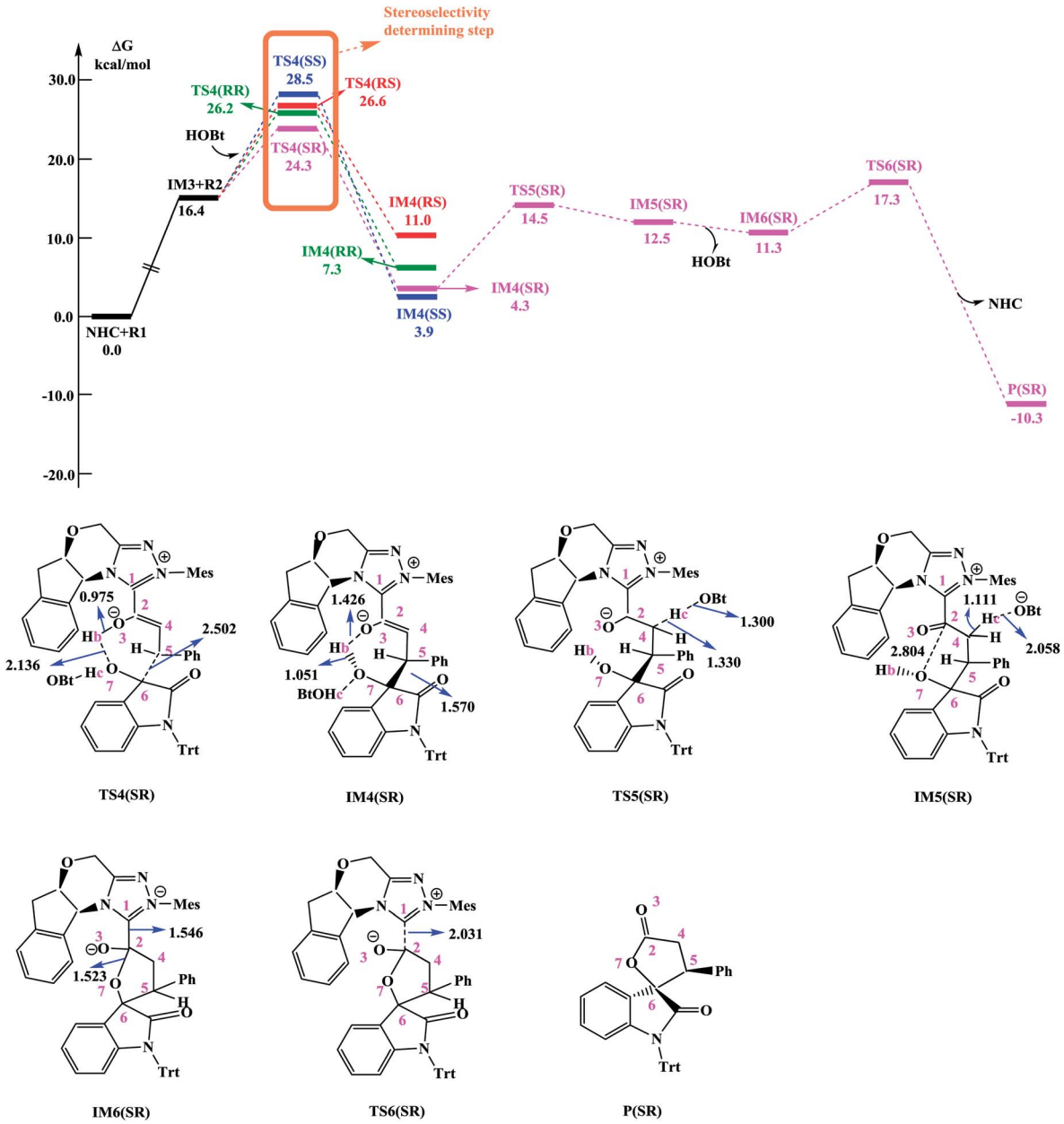

Fig. 2 Free energy profile obtained at SMD(THF)/M06-2X/6-311++G(d,p) level (kcal mol^{-1}) and optimized structures for steps IV–VI. Bbond lengths are given in Å.

TS4(SR) and **TS4(RS)**, which responsible for enantioselectivity, is 2.3 kcal mol^{-1} corresponding to an enantiomeric excess of 96%. The computed enantioselectivity is in good agreement with the experimental reported value (93%). Similarly, the energy difference between **TS4(SR)** and **TS4(RR)**, which is related to diastereoselectivity, is 1.9 kcal mol^{-1}. This energy difference corresponds to a diastereomeric ratio of 92%, which is in good agreement with the experimentally observed de of 91% (diastereomeric ratio > 20 : 1).

Furthermore, in order to better understand the origin of stereoselectivity of the **NHC**-catalyzed [3 + 2] annulation reaction, we performed the noncovalent interaction (NCI) analysis[21] which is demonstrated to be able to distinguish the strong interactions as well as the repulsion interactions. NCI analysis results for the stereoselectivity-determining transition states **TS3(RR)**, **TS3(RS)**, **TS3(SR)** and **TS3(SS)** are presented in Fig. 3. As depicted in Fig. 3, it is clear that a large green cloud between the π-systems of the **NHC**-bounded homoenolate (**IM3**-part) and HOBt is observed in **TS3(SR)**, but absent in the other transition states. In addition, the repulsion interactions exist in **TS3(RR)**, **TS3(RS)** and **TS3(SS)**. Moreover, a number of noncovalent interactions including π···π interactions, lone pair (LP)···π interactions and C–H···π interactions are identified in **TS3(SR)**. Therefore, **TS3(SR)** is more stable than the other transition states (**TS3(RR)**, **TS3(RS)** and **TS3(SS)**), which is in good agreement with the experimentally observed enantioselectivity.

Open Access Article. Published on 06 March 2019. Downloaded on 2/20/2026 12:47:03 PM.
This article is licensed under a Creative Commons Attribution-NonCommercial 3.0 Unported Licence.

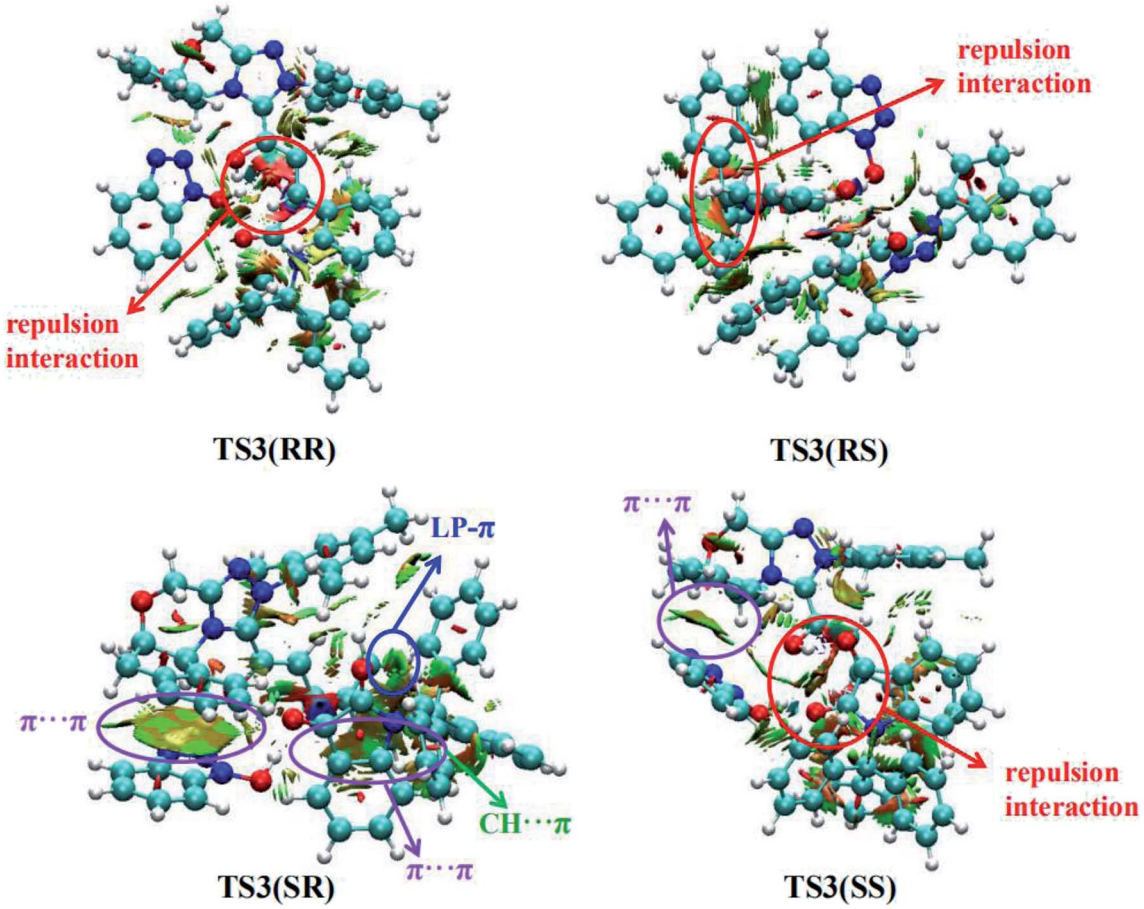

Fig. 3 Noncovalent interactions analysis (blue, strong interaction; green, weak interaction; and red, strong repulsion) for stereoselective transition states TS3(RR), TS3(RS), TS3(SR) and TS3(SS).

3.3 The nature of catalyst

In this section, global reactivity indexes (GRIs) analysis was carried out in order to understand the role of the **NHC** catalyst. The results are presented in Table 1. In GRI analysis, the molecular global electrophilicity character represented by the electrophilicity index ω, can be derived from the following expression, $\omega = (\mu^2/2\eta)$ (eV),[22] where μ and η are chemical potential and chemical hardness, respectively. μ and η can be calculated from the one-electron energies of the highest occupied molecular orbital (HOMO) and the lower unoccupied molecular orbital (LUMO), ε_H and ε_L with the expressions $\mu \approx (\varepsilon_H - \varepsilon_L)/2$ and $\eta \approx (\varepsilon_L - \varepsilon_H)$, respectively.[23] Within the Kohn–Sham scheme,[24] the empirical (relative) nucleophilicity index N[25] introduced by Domingo *et al.* was written as $N = \varepsilon_{H(Nu)} - \varepsilon_{H(TCE)}$. The nucleophilicity scale was referenced to tetracyanoethylene (TCE). Table 1 shows that from **R1** to **IM01**, the electronic chemical potential increases (−4.10 eV *vs.* −3.46 eV), which is consistent with what we found in NBO charge analysis, *i.e.*, the charge goes from **NHC** to **R1**. Table 1 also shows that the coupling of **NHC** catalyst with carboxylic esters **R1** strengthens its nucleophilicity (the nucleophilicities of **IM2** (4.96 eV) and **IM3** (5.40 eV) are larger than that of **R1**, N = 2.67 eV), but weakens its electrophilicity (the electrophilicity of **IM2** (**IM3**) is smaller than that of **R1**, 0.67 (0.79) eV *vs.* 1.10 eV). The GRI results suggest that the coordination of **NHC** to **R1** makes the nucleophilic addition to **R2** easier.

Table 1 Chemical hardness (η, in eV), electronic chemical potential, (μ, in eV), global electrophilicity, (ω, in eV), and global nucleophilicity (N, in eV) of selected structures involved in the NHC-catalyzed cycloaddition reaction

Species	η	μ	ω	N
R1	7.66	−4.10	1.10	2.67
IM01	7.05	−3.46	0.85	3.61
IM2	5.71	−2.77	0.67	4.96
IM3	4.85	−2.77	0.79	5.40

4. Conclusion

The reaction mechanism of the **NHC**-catalyzed cycloaddition reaction between carboxylic esters and isatins generating spirooxindole lactones with high enantio- and diastereoselectivities has been investigated by using density functional theory (DFT) calculations at SMD(THF)/M06-2X/6-311++G(d,p) level. The role of the additive HOBt is also examined in detail.

This journal is © The Royal Society of Chemistry 2019

Open Access Article. Published on 06 March 2019. Downloaded on 2/20/2026 12:47:03 PM.
This article is licensed under a Creative Commons Attribution-NonCommercial 3.0 Unported Licence.

The current computations reveal that the catalytic cycle comprises six steps: the **NHC** catalyst first attacks carboxylic ester, followed by α–C–H deprotonation gives the enolate intermediate. Subsequently, proton transfer occurs leading to the homoenolate intermediate and the next step is the stereoselective C–C bond formation. The fifth step is the generation of lactone intermediate and finally liberation of catalyst gives the cycloaddition product. DFT results reveal that the additive HOBt plays a critical role both in the proton transfer and in the stereoselective C–C formation. The activation barriers both for the proton transfer and for the stereoselective C–C bond formation are much lower in the presence of HOBt. The computed stereoselectivity in the presence of HOBt agrees very good with the experimentally reported enantioselectivity (computed 96%, experimental 93%) as well as diastereoselectivity (computed 92%, experimental 91%). The origin of stereoselectivity is traced to differential π···π stacking, C–H···π, lone pair (LP)···π and repulsion interactions that exist in the stereoselective-determining C–C bond formation transition state. These results should provide helpful insights for understanding the detailed reaction mechanism and the significant role of the HOBt additive.

Conflicts of interest

There are no conflicts of interest to declare.

Acknowledgements

This work is supported by the National Natural Science Foundation of China (No. 21403024), and National Supercomputing Center in Shenzhen.

References

1 (*a*) L. Wang, J. Xiao and T. P. Loh, *ChemCatChem*, 2014, **6**, 1183–1185; (*b*) K. J. R. Murauski, A. A. Jaworskia and K. A. Scheidt, *Chem. Soc. Rev.*, 2018, **47**, 1773–1782; (*c*) D. F. Chen, T. C. K. Chu and T. Rovis, *J. Am. Chem. Soc.*, 2017, **139**, 14897–14900.

2 (*a*) Z. G. Hajos and D. R. Parrish, *J. Org. Chem.*, 1974, **39**, 1615–1621; (*b*) B. List, R. A. Lerner and C. F. III Barbas, *J. Am. Chem. Soc.*, 2000, **122**, 2395–2396; (*c*) W. Notz, F. Tanaka and C. F. III Barbas, *Acc. Chem. Res.*, 2004, **37**, 580–591; (*d*) S. Mukherjee, J. W. Yang, S. Hoffmann and B. List, *Chem. Rev.*, 2007, **107**, 5471–5569; (*e*) A. J. B. Watson, D. W. C. Macmillan, Y. Wang, L. Deng, S. Shirakawa and K. Maruoka, in *Catalytic Asymmetric Synthesis*, ed. I. Ojima, John Wiley & Sons, Hoboken, NJ, 3rd edn, 2010, ch. 2, pp. 37–117.

3 (*a*) G. Yan and A. J. Borah, *Org. Chem. Front.*, 2014, **1**, 838–842; (*b*) Z. Huang and G. Dong, *Tetrahedron Lett.*, 2014, **55**, 5869–5889.

4 (*a*) F. Glorius, *N-heterocyclic carbene in catalysis – an introduction*, Springer-Verlag, Berlin, Heidelberg, 2006, vol. 21, p. 1; (*b*) S. P. Nolan, *Acc. Chem. Res.*, 2010, **44**, 91–100; (*c*) D. Zhang and G. F. Zi, *Chem. Soc. Rev.*, 2015, **44**, 1898–1921; (*d*) C. Chen, M. H. Kim and S. H. Hong, *Org. Chem. Front.*, 2015, **2**, 241–247.

5 (*a*) D. Enders, O. Niemeier and A. Henseler, *Chem. Rev.*, 2007, **107**, 5606–5655; (*b*) F. Glorius and K. Hirano, *Nucleophilic carbenes as organocatalysts*, Springer-Verlag, Berlin, Heidelberg, 2008, vol. 2, p. 159; (*c*) J. L. Moore and T. Rovis, *Top. Curr. Chem.*, 2010, **291**, 77–144; (*d*) D. Enders and T. Balensiefer, *Acc. Chem. Res.*, 2004, **37**, 534–541; (*e*) V. Nair, S. Vellalath and B. P. Babu, *Chem. Soc. Rev.*, 2008, **37**, 2691–26981; (*f*) M. Fèvre, J. Pinaud, Y. Gnanou, J. Vignolle and D. Taton, *Chem. Soc. Rev.*, 2013, **42**, 2142–2172.

6 (*a*) M. He, J. R. Struble and J. W. Bode, *J. Am. Chem. Soc.*, 2006, **128**, 8418–8420; (*b*) J. J. Song, Z. Tan, J. T. Reeves, N. K. Yee and C. H. Senanayake, *Org. Lett.*, 2007, **9**, 1013–1016; (*c*) D. A. DiRocco, K. M. Oberg, D. M. Dalton and T. Rovis, *J. Am. Chem. Soc.*, 2009, **131**, 10872–10874; (*d*) Y. Kayaki, M. Yamamoto and T. Ikariya, *Angew. Chem., Int. Ed.*, 2009, **48**, 4194–4197; (*e*) D. Enders, A. Grossmann, J. Fronert and G. Raabe, *Chem. Commun.*, 2010, **46**, 6282–6284; (*f*) J. Kaeobamrung, M. C. Kozlowski and J. W. Bode, *Proc. Natl. Acad. Sci. U. S. A.*, 2010, **107**, 20661–20665; (*g*) D. E. A. Raup, B. Cardinal-David, D. Holte and K. A. Scheidt, *Nat. Chem.*, 2010, **2**, 766–771; (*h*) Q. Kang and Y. Zhang, *Org. Biomol. Chem.*, 2011, **9**, 6715–6719; (*i*) S. J. Ryan, L. Candish and D. W. Lupton, *J. Am. Chem. Soc.*, 2011, **133**, 4694–4697; (*j*) T. Jousseaume, N. E. Wurz and F. Glorius, *Angew. Chem., Int. Ed.*, 2011, **50**, 1410–1414; (*k*) D. A. DiRocco and T. Rovis, *J. Am. Chem. Soc.*, 2011, **133**, 10402–10405; (*l*) Z. Fu, J. Xu, T. Zhu, W. W. Y. Leong and Y. R. Chi, *Nat. Chem.*, 2013, **5**, 835–839; (*m*) J. Chen and Y. Huang, *Nat. Commun.*, 2014, **5**(1–8), 3437; (*n*) Z. Jin, S. Chen, Y. Wang, P. Zheng, S. Yang and Y. R. Chi, *Angew. Chem., Int. Ed.*, 2014, **53**, 13506–13509; (*o*) V. Yatham, J. M. Neudörfl, N. E. Schlörer and A. Berkessel, *Chem. Sci.*, 2015, **6**, 3706–3710; (*p*) B. S. Li, Y. Wang, Z. Jin, P. Zheng, R. Ganguly and Y. R. Chi, *Nat. Commun.*, 2015, **6**, 6207–6211; (*q*) C. Guo, M. Fleige, D. Janssen-Müller, C. G. Daniliuc and F. Glorius, *Nat. Chem.*, 2015, **7**, 842–848; (*r*) K. Yamashita, S. Hase, Y. Kayaki and T. Ikariya, *Org. Lett.*, 2015, **17**, 2334–2337; (*s*) Y. Nakano and D. W. Lupton, *Angew. Chem., Int. Ed.*, 2016, **55**, 3135–3139; (*t*) C. Zhao, F. Li and J. Wang, *Angew. Chem., Int. Ed.*, 2016, **55**, 1820–1824; (*u*) S. R. Yetra, S. Mondal, S. Mukherjee, R. G. Gonnade and A. T. Biju, *Angew. Chem., Int. Ed.*, 2016, **55**, 268–272.

7 (*a*) X. N. Wang, P. L. Shao, H. Lv and S. Ye, *Org. Lett.*, 2009, **11**, 4029–4032; (*b*) X. L. Huang, X. Y. Chen and S. Ye, *J. Org. Chem.*, 2009, **74**, 7585–7587; (*c*) J. Douglas, J. E. Taylor, G. Churchill, A. M. X. Slawin and A. D. Smith, *J. Org. Chem.*, 2013, **78**, 3925–3938; (*d*) X. N. Wang, L. T. Shen and S. Ye, *Org. Lett.*, 2011, **13**, 6382–6385; (*e*) T. Wang, X. L. Huang and S. Ye, *Org. Biomol. Chem.*, 2010, **8**, 5007–5010; (*f*) H. M. Zhang, Z. H. Gao and S. Ye, *Org. Lett.*, 2014, **16**, 3079–3081.

8 (*a*) X. Q. Fang, X. K. Chen and Y. R. Chi, *Org. Lett.*, 2011, **13**, 4708–4711; (*b*) L. M. Fang, F. Wang, P. J. Chua, Y. B. Lv, L. J. Zhong and G. F. Zhong, *Org. Lett.*, 2012, **14**, 2894–2897.

Open Access Article. Published on 06 March 2019. Downloaded on 2/20/2026 12:47:03 PM. This article is licensed under a Creative Commons Attribution-NonCommercial 3.0 Unported Licence.

9 (*a*) H. Lu, J. Y. Liu, C. G. Li, J. B. Lin, Y. M. Liang and P. F. Xu, *Chem. Commun.*, 2015, **51**, 4473–4476; (*b*) S. H. Hu, B. Y. Wang, Y. Zhang, W. F. Tang, M. Y. Fang, T. Lu and D. Du, *Org. Biomol. Chem.*, 2015, **13**, 4661–4667; (*c*) S. R. Yetra, S. Mondal, E. Suresh and A. T. Biju, *Org. Lett.*, 2015, **17**, 1417–1420; (*d*) J. D. Tessier, E. A. O'Bryan, T. B. H. Schroeder, D. T. Cohen and K. A. Scheidt, *Angew. Chem., Int. Ed.*, 2012, **124**, 5047–5051; (*e*) Z. Q. Liang, Z. H. Guo, W. Q. Jia and S. Ye, *Chem.–Eur. J.*, 2015, **21**, 1868–1872; (*f*) C. Guo, M. Schedler, C. G. Daniliuc and F. Glorius, *Angew. Chem., Int. Ed.*, 2014, **53**, 10232–10236; (*g*) A. G. Kravina, J. Mahatthananchai and J. W. Bode, *Angew. Chem., Int. Ed.*, 2012, **51**, 9433–9436; (*h*) Y. Zhang, Y. Y. Lu, W. F. Tang, T. Lu and D. Du, *Org. Biomol. Chem.*, 2014, **12**, 3009–3015.

10 (*a*) J. Izquierdo, A. Orue and K. A. Scheidt, *J. Am. Chem. Soc.*, 2013, **135**, 10634–10637; (*b*) Y. W. Xie, Y. L. Que, T. J. Li, L. Zhu, C. X. Yu and C. S. Yao, *Org. Biomol. Chem.*, 2015, **13**, 1829–1835; (*c*) H. Lv, W. Q. Jia, L. H. Sun and S. Ye, *Angew. Chem., Int. Ed.*, 2013, **125**, 8769–8772.

11 F. Xu, S. R. Yuan, M. Z. Miao and Z. K. Chen, *J. Org. Chem.*, 2016, **81**, 11454–11460.

12 Y. Zhao and D. G. Truhlar, *Theor. Chem. Acc.*, 2007, **120**, 215–241.

13 (*a*) H. Xue, D. Jiang, H. Jiang, C. W. Kee, H. Hirao, T. Nishimura, M. W. Wong and C. H. Tan, *J. Org. Chem.*, 2015, **80**, 5745–5752; (*b*) M. W. Wong and A. M. E. Ng, *Aust. J. Chem.*, 2014, **67**, 1100–1109; (*c*) H. Yang and M. W. Wong, *J. Am. Chem. Soc.*, 2013, **135**, 5808–5818; (*d*) E. H. Krenske, E. C. Davison, I. T. Forbes, J. A. Warner, A. L. Smith, A. B. Holmes and K. N. Houk, *J. Am. Chem. Soc.*, 2012, **134**, 2434–2441; (*e*) H. Yang and M. W. Wong, *J. Org. Chem.*, 2011, **76**, 7399–7405; (*f*) Y. Zhao and D. G. Truhlar, *Acc. Chem. Res.*, 2008, **41**, 157–167.

14 C. Gonzalez and H. B. Gonzalez, *J. Phys. Chem.*, 1990, **94**, 5523–5527.

15 A. V. Marenich, C. J. Cramer and D. G. Truhlar, *J. Phys. Chem. B*, 2009, **113**, 6378–6396.

16 (*a*) E. D. Glendening, A. E. Reed, J. E. Carpenter and F. Weinhold, *NBO Version 3.1*, Theoretical Chemistry Institute, University of Wisconsin, Madison, WI, 1996; (*b*) A. E. Reed, L. A. Curtiss and F. Weinhold, *Chem. Rev.*, 1988, **88**, 899–926; (*c*) J. P. Foster and F. Weinhold, *J. Am. Chem. Soc.*, 1980, **102**, 7211–7218.

17 M. J. Frisch, G. W. Trucks, H. B. Schlegel, G. E. Scuseria, M. A. Robb, J. R. Cheeseman, G. Scalmani, V. Barone, B. Mennucci, G. A. Petersson, H. Nakatsuji, M. Caricato, X. Li, H. P. Hratchian, A. F. Izmaylov, J. Bloino, G. Zheng, J. L. Sonnenberg, M. Hada, M. Ehara, K. Toyota, R. Fukuda, J. Hasegawa, M. Ishida, T. Nakajima, Y. Honda, O. Kitao, H. Nakai, T. Vreven, J. A. Montgomery, Jr., J. E. Peralta, F. Ogliaro, M. Bearpark, J. J. Heyd, E. Brothers, K. N. Kudin, V. N. Staroverov, T. Keith, R. Kobayashi, J. Normand, K. Raghavachari, A. Rendell, J. C. Burant, S. S. Iyengar, J. Tomasi, M. Cossi, N. Rega, J. M. Millam, M. Klene, J. E. Knox, J. B. Cross, V. Bakken, C. Adamo, J. Jaramillo, R. Gomperts, R. E. Stratmann, O. Yazyev, A. J. Austin, R. Cammi, C. Pomelli, J. W. Ochterski, R. L. Martin, K. Morokuma, V. G. Zakrzewski, G. A. Voth, P. Salvador, J. J. Dannenberg, S. Dapprich, A. D. Daniels, O. Farkas, J. B. Foresman, J. V. Ortiz, J. Cioslowski and D. J. Fox, *Gaussian 09 (Revision D.01)*, Gaussian, Inc., Wallingford CT, 2013.

18 (*a*) Q. Zhang, H. Z. Yu and Y. Fu, *Org. Chem. Front.*, 2014, **1**, 614–624; (*b*) J. Mahatthananchai and J. W. Bode, *Acc. Chem. Res.*, 2013, **47**, 696–707.

19 (*a*) Y. Wang, D. Wei, Y. Wang, W. Zhang and M. Tang, *ACS Catal.*, 2016, **6**, 279–289; (*b*) Y. Wang, D. Wei and M. Tang, *J. Org. Chem.*, 2017, **82**, 13043–13050; (*c*) Y. Wang, Y. Qiao, D. Wei and M. Tang, *Org. Chem. Front.*, 2017, **4**, 1987–1998; (*d*) Y. Wang, D. Wei and W. Zhang, *ChemCatChem*, 2018, **10**, 338–360.

20 D. Y. Curtin, *Rec. Chem. Prog.*, 1954, **15**, 111–128.

21 T. Lu and F. W. Chen, *J. Comput. Chem.*, 2012, **33**, 580–592.

22 R. G. Parr, L. V. Szentpály and S. Liu, *J. Am. Chem. Soc.*, 1999, **121**, 1922–1924.

23 (*a*) R. G. Parr and W. Yang, *Density Functional Theory of Atoms and Molecules*, Oxford University Press, New York, 1989; (*b*) R. G. Parr and R. G. Pearson, *J. Am. Chem. Soc.*, 1983, **105**, 7512–7516.

24 W. S. Kohn and L. J. Sham, *Phys Rev.*, 1965, **140**, 1133–1138.

25 L. R. Domingo, E. Chamorro and P. Pérez, *J. Org. Chem.*, 2008, **73**, 4615–4624.

This journal is © The Royal Society of Chemistry 2019